Wavelet-Based Multiresolution Local Tomography

Farrokh Rashid-Farrokhi, *Student Member, IEEE,* K. J. Ray Liu, *Senior Member, IEEE,*
Carlos A. Berenstein, and David Walnut

Abstract—We develop an algorithm to reconstruct the wavelet coefficients of an image from the Radon transform data. The proposed method uses the properties of wavelets to localize the Radon transform and can be used to reconstruct a local region of the cross section of a body, using almost completely local data that significantly reduces the amount of exposure and computations in X-ray tomography. The property that distinguishes our algorithm from the previous algorithms is based on the observation that for some wavelet bases with sufficiently many vanishing moments, the ramp-filtered version of the scaling function as well as the wavelet function has extremely rapid decay. We show that the variance of the elements of the null-space is negligible in the locally reconstructed image. Also, we find an upper bound for the reconstruction error in terms of the amount of data used in the algorithm. To reconstruct a local region 16 pixels in radius in a 256×256 image, we require 22% of full exposure data.

Index Terms—Local tomography, multiresolution tomography, wavelet.

I. INTRODUCTION

IT IS WELL KNOWN that in dimension two and in fact in any even dimension, the Radon transform is not local, that is, the recovery of an image at any fixed point requires the knowledge of all projections of the image. This means that a patient would have to be exposed to a relatively large amount of X-rays even if it was desired to view only a small part of the patient's body. Thus, searching for a means to reduce exposure, and at the same time to be able to perfectly reconstruct the region of interest (ROI), has been of great interest recently [6]–[11].

The application of wavelet theory to the inversion of the Radon transforms was first proposed in [3] and [4]. An inversion formula based on the continuous wavelet transform was proposed in [1]. This formula was based on an intertwining between the one-dimensional (1-D) continuous wavelet transform of the projection data at each angle and the two-dimensional (2-D) wavelet transform of the original image. The fundamental observation was that the admissibility or vanishing moment condition that is characteristic of a wavelet is preserved under the Hilbert transform. Moreover (as was noted in [2] and [8]), the Hilbert transform of a function with many vanishing moments should decay very rapidly. This is related to the notion that certain singular integral operators are almost diagonalized by wavelets [20]. In [2], the intertwining formula of [1] was used for local recovery, and explicit error estimates on the recovered image within the ROI were obtained. It was noted that high-frequency features of an image can be recovered locally using the wavelet transform.

The first numerical algorithm using wavelets for local reconstruction was implemented by DeStefano and Olson in [8]. This algorithm reconstructs the local values of a function f directly from the 1-D wavelet transform of $R_\theta f$ at each angle θ. In [9], Delaney and Bresler compute the 2-D separable wavelet transform of a function directly from the projection data as a means to do local recovery from local measurements. Both algorithms take advantage of the observation that the Hilbert transform of a function with many vanishing moments has rapid decay; and both algorithms recover the high-resolution parts of the image locally (that is, by exposing the ROI plus a small extra margin) and obtain the low-resolution parts by global measurements at a few angles. In this sense, these algorithms cannot accurately be described as local tomography algorithms. Both of these algorithms exhibit similar savings in exposure and similar quality of the reconstructed image in the ROI. Recently, Olson [11] has improved his algorithm by replacing the usual wavelet transform with the local trigonometric transform of Coifman and Meyer [14] and has reduced the exposure still further.

In this paper, we implement a wavelet-based algorithm to reconstruct a good approximation of the low-resolution parts of the image as well as the high-resolution parts using only local measurements. The algorithm is based on the observation that in some cases, the Hilbert transform of a compactly supported *scaling function* also has essentially the same support as the scaling function itself. This phenomena is related to the number of vanishing moments of the scaling function of an orthonormal or biorthonormal wavelet basis. That is, if $\phi(t)$ is such a scaling function, and if $\hat{\phi}^{(j)}(0) = 0$ for $j = 1, 2, \cdots, K$, for some large K, then the Hilbert transform of ϕ will have rapid decay. This gives substantial savings in exposure and computation compared to the methods in [8] and [9], and somewhat greater exposure (though still fewer computations) than the algorithm in [11]. Our algorithm reconstructs a region of radius 16 pixels in a 256×256 image to within 1% average error using 22% of the data, and to within 1% maximum error using 30% of the data. The methods proposed in [8] and [9] require a higher exposure of 40% of the data for the same

size region and 1% maximum error, and the method in [11] uses 20% for the same case. Since the algorithm in [11] is not truly local, we believe that our algorithm is valuable even if the exposure is somewhat higher.

It should be noted that the goal of the algorithm described in this paper is to reconstruct the function locally from local measurements *up to the nullspace* of the interior Radon transform. That is, the problem of recovery of local values of a function from local projections only is not uniquely solvable [22]–[25]. In [23], an example is given of functions that are nonzero on a disk but whose projections on all lines intersecting that disk are zero (Fig. 7). Such a function is said to be an element of the nullspace of the interior Radon transform. Any algorithm that uses only local measurements cannot reconstruct these nullspace elements. The advantage is that taking only local measurements is much easier to implement in hardware. It has been shown that the elements of the null-space of the interior Radon transform do not vary much in the ROI [23]. In our algorithm this phenomenon appears as a constant bias in the reconstructed image. Such a bias is commonly observed in the local reconstruction problem [23], [25].

The algorithms of DeStefano/Olson [8], Delaney/Bresler [9], and Olson [11] are not true local tomography algorithms in that they use measurements far from the ROI to recover the function exactly on the ROI. The algorithm described in this paper is more closely related to the technique of Λ-tomography, which is used to reconstruct the function $\Lambda f - \mu \Lambda^{-1} f$ rather than the density function f [5], [6]. The function Λf has the same singularities as f and is cupped where f is constant. The addition of the cup correction factor $\mu \Lambda^{-1} f$ results in good qualitative reconstructions of f [7].

In this paper, we will present an algorithm to reconstruct the wavelet and scaling coefficients of an image directly from its projections. This is useful in applications where the wavelet coefficients of the reconstructed image are used, in that it saves the computations required to obtain the wavelet coefficients from the reconstructed image. We also show how this reconstruction technique leads to a local tomography algorithm that uses the projections of the image on lines intersecting the local ROI plus a small number of projections, in the immediate vicinity, to obtain a very good approximation of the image in the ROI.

The main features of our algorithm are as follows.

- It has *reduced exposure* compared to previous algorithms (cf. [8], [9]), though the exposure is increased when compared to [11]. In our algorithm there is no need to obtain a rough estimate of the global properties of the Radon transform by sparsely sampled full exposure projections. We just compute a small number of projections on lines passing close to the ROI to reconstruct the local values of the image up to a constant bias. Moreover, the number of pixels in the margin is independent of the size of the ROI and is also independent of the resolution of the measurements taken. Therefore, for the same ROI, a high resolution computerized tomography (CT) scan would have a smaller region of exposure than a lower resolution scan (see Figs. 13 and 14).

- It is *computationally more efficient* than other algorithms, because it uses fewer projections overall to locally reconstruct the image.
- It offers *uniform exposure at all angles*, which allows for easier implementation in hardware. (In the algorithms proposed in [8]–[11], different amount of projections have to be computed with variable lengths for different angles.)
- It offers the *ability to reconstruct off-center or even multiple regions of interest*, as well as centered reconstruction.
- It is *applicable to the cases where the wavelet basis is not separable* and there exists no multiresolution approach to obtain the wavelet coefficients. (The method proposed in [9] can only be used for separable wavelet bases.)
- It allows for *reconstruction of the wavelet coefficients* of the image with the same complexity as the conventional filtered backprojection method.

This paper is organized as follows. In Section II, we will briefly introduce the Radon transform, discuss the nonlocality of the Radon transform and the conventional reconstruction technique, i.e., the filtered backprojection method. In Section III after reviewing the basics of the wavelet transform, we will introduce a full-data reconstruction technique based on the wavelet transform. We will discuss the locality property of the proposed algorithm in Section IV. Section V then discusses the implementation of this method, and in Section VI the simulation results will be presented.

II. PRELIMINARIES AND NOTATIONS

In this section, we will briefly introduce the terminology and definitions required in the subsequent discussions. In this paper, we use the following notations. The d dimensional Euclidean space is denoted by R^d. Given a set $S \subset R^d$, $\mathbf{1}_S$ denotes the indicator function of S. We define the Fourier transform in R^d by $\hat{f}(\vec{\omega}) = \int_{R^d} f(\vec{x}) e^{j2\pi \vec{\omega} \cdot \vec{x}} d\vec{x}$. The inverse Fourier transform is defined by $f(\vec{x}) = (\hat{f})^\vee(\vec{x}) = \int_{R^d} \hat{f}(\vec{\omega}) e^{-j2\pi \vec{\omega} \cdot \vec{x}} d\vec{\omega}$. Both continuous and discrete convolution operators are denoted by $*$.

A. Radon Transform

In CT, a cross section of a human body is scanned by a nondiffracting thin X-ray beam whose intensity loss is recorded by a set of detectors. The Radon transform (RT) is a mathematical tool that is used to describe the recorded intensity losses as averages of the tissue density function over hyperplanes which, in dimension two, are lines. Given $f(\vec{x})$, restricted to a disc of radius one, we define the Radon transform of f by

$$R_\theta f(s) = \int_{\vec{x} \cdot \vec{\theta} = s} f(\vec{x}) \, d\vec{x} = \int_{\theta \perp} f(s\vec{\theta} + y) \, dy$$

where $\vec{\theta} = (\cos\theta, \sin\theta), \theta \in [0, 2\pi), s \in R$ and $\theta^\perp$ is the subspace perpendicular to $\vec{\theta}$.

The interior Radon transform [24], [25] is the Radon transform restricted to lines passing through the ROI, which is a circle of radius r $(r < 1)$ about the origin. It is defined by

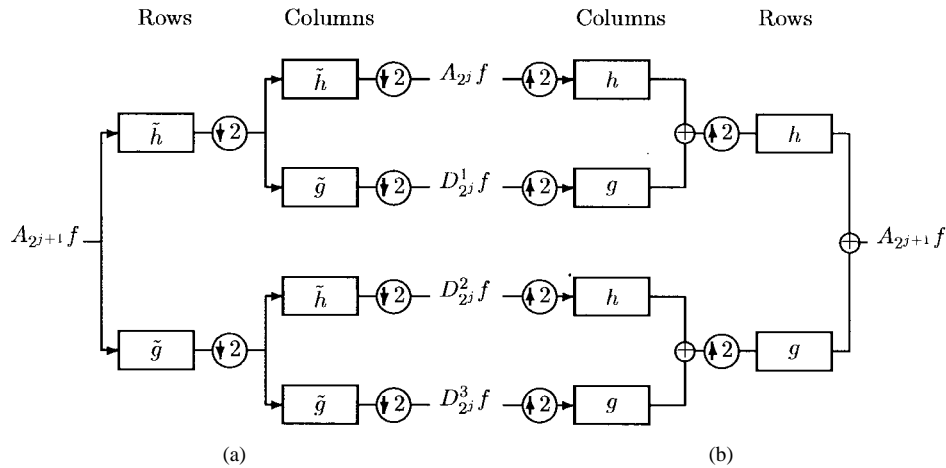$$R_\theta f(s) \to R_\theta f(s) \mathbf{1}_{[-r, r]}(s).$$

Fig. 1.   (a) Wavelet analysis filterbank. (b) Wavelet synthesis filterbank.

The problem of recovery of f from the interior Radon transform is called the *interior problem* or *region of interest tomography*. The interior problem in dimension two is not uniquely solvable, i.e., there are functions that are not zero in the ROI but whose projections on lines intersecting that region are zero. However, these functions do not vary much inside the ROI, and in fact a crude approximation to the missing projections suffices to approximate f well inside the region of interest up to an additive constant [23].

B. Reconstruction

The basic formula for inverting the Radon transform is based on the fact that the Fourier transform of the Radon transform with respect to the variable s is the Fourier transform of the function f along a line passing through the origin. This property is known as the projection theorem or Fourier slice theorem, as follows:

$$(\widehat{R_\theta f})(\omega) = \hat{f}(\omega\vec{\theta}), \qquad \omega \in R.$$

Thus, the Fourier transform of the projections at enough angles could in principle be assembled into a complete description of the 2-D Fourier transform of the image and then simply inverted to arrive at the function f. Using the polar Fourier inversion formula and the Fourier slice theorem, we can reconstruct the function f from the projection data $R_\theta f(s)$ by

$$f(\vec{x}) = \int_0^\pi \int_{-\infty}^\infty (\widehat{R_\theta f})(\omega) e^{j2\pi\omega(\vec{x}\cdot\vec{\theta})} |\omega| \, d\omega \, d\theta. \qquad (1)$$

The above formula, called the filtered backprojection formula, can be implemented in two steps, the filtering step, which in the Fourier domain can be written as

$$\hat{Q}_\theta(\omega) = \widehat{R_\theta f}(\omega)|\omega| \qquad (2)$$

and the backprojection step

$$f(\vec{x}) = \int_0^\pi Q_\theta(\vec{x}\cdot\vec{\theta}) \, d\theta. \qquad (3)$$

Because $|\omega|$ is not bounded and filtering by this filter tends to magnify the high-frequency noise, it is expedient in practice to multiply this operator by a smoothing window $W(\omega)$ as

$$\hat{Q}_\theta(\omega) = \widehat{R_\theta f}(\omega)|\omega|W(\omega). \qquad (4)$$

Therefore, the reconstruction will result in an approximation of f rather than f itself. Normally the approximation has the form $e * f$, where e is an approximate delta function, called the point spread function (psf) [18]. The psf e is related to $W(\omega)$ by

$$W(\omega) = \hat{e}(\omega\cos\theta, \omega\sin\theta).$$

C. Nonlocality of RT Inversion

In (2), the Radon transform data is filtered by $|\omega|$. This operation can be formulated in the space domain as

$$Q_\theta(t) = H\partial R_\theta f(t),$$

where H is the Hilbert transform on R, and ∂ is ordinary differentiation. In the above equation the derivative part is a local operator, but the Hilbert transform

$$(\widehat{Hg})(\omega) = i\,\mathrm{sign}\,(\omega)\hat{g}(\omega) \qquad (5)$$

introduces a discontinuity in the derivative of the Fourier transform of a function at the origin. Hence, the Hilbert transform of a compactly supported function can never be compactly supported. This means that RT inversion based on (1) can not be accomplished locally; that is, in order to recover f exactly at a point $\vec{x}$, all projections of f are required and not just those on lines passing near $\vec{x}$. It has been noted that the above mentioned filtering will not increase the essential support of a function if the function's Fourier transform vanishes to high order at the origin [2], [8]. Wavelets that are in general constructed with as many zero moments as possible are good candidates for these functions.

III. WAVELET RECONSTRUCTION

A. Continuous Wavelet Transform

The wavelet transform has been an increasingly popular tool for signal and image processing. The transform decomposes
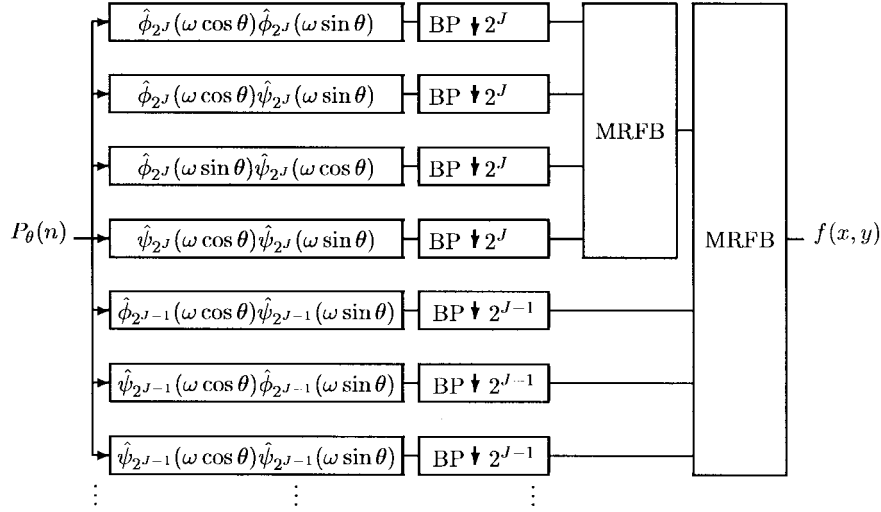
Fig. 2. Wavelet reconstruction from projection data; the multiresolution reconstruction filterbank (MRFB) is the wavelet synthesis filterbank (Fig. 1).

the signal onto shifts and dilates of a function called the mother wavelet. In two dimensions, the wavelet transform is defined as follows. Let $g(\vec{t}), \vec{t} \in R^2$ satisfy

$$0 < \inf_{\theta \in [0, 2\pi)} \int_0^\infty r^{-1} |\hat{g}(r \cos \theta, r \sin \theta)|^2 \, dr$$
$$< \sup_{\theta \in [0, 2\pi)} \int_0^\infty r^{-1} |\hat{g}(r \cos \theta, r \sin \theta)|^2 \, dr < \infty. \quad (6)$$

Let $\tilde{g}(\vec{t}) = g(-\vec{t}), \vec{t} \in R^2$, and define the continuous wavelet transform of f, on R^2, by

$$W_u^{(2)}(g; f)(\vec{v}) = \int_{R^2} f(\vec{t}) u g(u\vec{t} - \vec{v}) \, d\vec{t}$$
$$= f * \tilde{g}_u(u^{-1}\vec{v}) \quad (7)$$

where $u \in R \backslash \{0\}$ and $\vec{v} = [x \quad y] \in R^2$, and $g_u(\vec{v}) = u g(u\vec{v})$. In order to reconstruct the function f from its wavelet transform, we use

$$f(\vec{t}) = \int_{R^2} \int_R u^4 W_u^{(2)}(g; f)(\vec{v}) g(u\vec{t} - \vec{v}) \, du \, d\vec{v}.$$

B. Multiresolution Wavelet Representation

In practice, one prefers to write f as a discrete superposition of wavelets, therefore we define the discrete wavelet transform by

$$W_{2^j}^{(2)}(g; f)(\vec{n}) = \int_{R^2} f(\vec{t}) g_{2^j}(\vec{t} - 2^{-j} \vec{n}) \, d\vec{t}$$

which is derived from (7) by setting $u = 2^j$ and $\vec{v} = \vec{n}$, where $j \in Z$ and $\vec{n} \in Z^2$.

Below we describe a multiresolution analysis approach to recovering $f(\vec{x})$ from its discrete wavelet transform (precise definitions and further details can be found in [17]). Let A_{2^j} be the operator that approximates a measurable function $f(\vec{x})$ with finite energy ($f(\vec{x}) \in L^2(R^2)$) at resolution 2^j. We consider the vector space $V_{2^j} \subset L^2(R^2)$ as the set of all possible approximations at the resolution 2^j of functions in $L^2(R^2)$, such that $\forall j \in Z, V_{2^j} \subset V_{2^{j+1}}$. For

each multiresolution approximation V_{2^j}, there exists a unique function $\phi(x) \in L^2(R)$, called a scaling function. Let $h(n) = \langle \phi_{2^{-1}}(u), \phi(u - n) \rangle$, the Fourier transform of $h(n)$, denoted by $H(\omega)$, is defined as

$$H(\omega) = \sum_{n=-\infty}^{\infty} h(n) e^{-jn\omega}.$$

The Fourier transform of $\phi(x)$ is given by

$$\hat{\phi}(\omega) = \prod_{p=1}^{\infty} H(2^{-p}\omega)$$

and

$$\hat{\phi}_{2^j}(\omega) = \hat{\phi}(\omega) \prod_{p=1}^{j} H(2^{1-p}\omega).$$

Define the function $\psi(x)$, the mother wavelet, by $\hat{\psi}(\omega) = G(\omega/2)\hat{\phi}(\omega/2)$, where $G(\omega) = e^{-j\omega}\overline{H(\omega + \pi)}$. It can be shown that

$$\hat{\psi}_{2^j}(\omega) = \begin{cases} \hat{\phi}(\omega) G(2^{j-1}\omega) \prod_{p=1}^{j-1} H(2^{1-p}\omega), & \text{if } j > 1 \\ \hat{\phi}(\omega) G(\omega), & \text{if } j = 1. \end{cases}$$

Letting $\Phi(x, y) = \phi(x)\phi(y)$

$$\{\Phi_{2^j}(x - 2^{-j}n, y - 2^{-j}m)\}_{(n,m) \in Z^2} \quad (8)$$

forms an orthonormal basis for V_{2^j}, in a multiresolution approximation in $L^2(R^2)$, where $\Phi_{2^j}(x, y) = 2^j \Phi(2^j x, 2^j y) = \phi_{2^j}(x)\phi_{2^j}(y) = 2^{j/2}\phi(2^j x) \cdot 2^{j/2}\phi(2^j x)$. The projection of f onto V_{2^j} can therefore be computed in this case by

$$A_{2^j} f(x, y)$$
$$= \sum_{n=-\infty}^{\infty} \sum_{m=-\infty}^{\infty} \langle f(u, v), \phi_{2^j}(u - 2^{-j}n)\phi_{2^j}(v - 2^{-j}m) \rangle$$
$$\cdot \phi_{2^j}(x - 2^{-j}n)\phi_{2^j}(y - 2^{-j}m).$$

The discrete approximation at resolution 2^j is defined by

$$A_{2^j}^d f(n,m) = (f(u,v) * \tilde{\phi}_{2^j}(u)\tilde{\phi}_{2^j}(v))(2^{-j}n, 2^{-j}m) \quad (9)$$

where $(n,m) \in Z^2$ and $\tilde{\phi}_{2^j}(u) = \phi_{2^j}(-u)$. The difference between the approximation $A_{2^j}f(x,y)$ and $A_{2^{j+1}}f(x,y)$, called the detail signal at resolution 2^j, corresponds to the projection of f on the orthogonal complement of V_{2^j} in $V_{2^{j+1}}$, denoted by O_{2^j}. Let

$$\Psi^1(x,y) = \phi(x)\psi(y), \quad \Psi^2(x,y) = \psi(x)\phi(y)$$
$$\Psi^3(x,y) = \psi(x)\psi(y) \quad (10)$$

then the set of functions

$$\{\Psi_{2^j}^1(x - 2^{-j}n, y - 2^{-j}m), \Psi_{2^j}^2(x - 2^{-j}n, y - 2^{-j}m),$$
$$\Psi_{2^j}^3(x - 2^{-j}n, y - 2^{-j}m)\}_{(n,m) \in Z^2},$$

where $\Psi_{2^j}^i(x,y) = 2^j \Psi^i(2^j x, 2^j y)$ is an orthonormal basis for O_{2^j}. The projection of $f(x,y)$ on the vector space O_{2^j} is given by

$$D_{2^j,1} f(x,y)$$
$$= \sum_{n=-\infty}^{\infty} \sum_{m=-\infty}^{\infty} \langle f(u,v), \phi_{2^j}(u - 2^{-j}n)\psi_{2^j}(v - 2^{-j}m) \rangle$$
$$\cdot \phi_{2^j}(x - 2^{-j}n)\psi_{2^j}(y - 2^{-j}m)$$

$$D_{2^j,2} f(x,y)$$
$$= \sum_{n=-\infty}^{\infty} \sum_{m=-\infty}^{\infty} \langle f(u,v), \psi_{2^j}(u - 2^{-j}n)\phi_{2^j}(v - 2^{-j}m) \rangle$$
$$\cdot \psi_{2^j}(x - 2^{-j}n)\phi_{2^j}(y - 2^{-j}m)$$

$$D_{2^j,3} f(x,y)$$
$$= \sum_{n=-\infty}^{\infty} \sum_{m=-\infty}^{\infty} \langle f(u,v), \psi_{2^j}(u - 2^{-j}n)\psi_{2^j}(v - 2^{-j}m) \rangle$$
$$\cdot \psi_{2^j}(x - 2^{-j}n)\psi_{2^j}(y - 2^{-j}m).$$

The detail coefficients are given by

$$D_{2^j,1}^d f(n,m)$$
$$= (f(x,y) * 2^{-j}\tilde{\phi}_{2^j}(x)\tilde{\psi}_{2^j}(y))(2^{-j}n, 2^{-j}m)$$
$$D_{2^j,2}^d f(n,m)$$
$$= (f(x,y) * 2^{-j}\tilde{\psi}_{2^j}(x)\tilde{\phi}_{2^j}(y))(2^{-j}n, 2^{-j}m)$$
$$D_{2^j,3}^d f(n,m)$$
$$= (f(x,y) * 2^{-j}\tilde{\psi}_{2^j}(x)\tilde{\psi}_{2^j}(y))(2^{-j}n, 2^{-j}m) \quad (11)$$

where $(n,m) \in Z^2$ and $\tilde{\psi}_{2^j}(u) = \psi_{2^j}(-u)$. Fig. 1(a) shows the conventional filterbank, which is usually used to obtain approximation and details of a signal.

The discrete approximation at resolution 2^{j+1} can be obtained by combining the detail and approximation at resolution 2^j, i.e.,

$$A_{2^{j+1}}^d f(n,m)$$
$$= 2 \sum_{k=-\infty}^{\infty} \sum_{l=-\infty}^{\infty} h(n - 2k)h(m - 2l)A_{2^j}^d f(k,l)$$
$$+ 2 \sum_{k=-\infty}^{\infty} \sum_{l=-\infty}^{\infty} h(n - 2k)g(m - 2l)D_{2^j,1}^d f(k,l)$$

$$+ 2 \sum_{k=-\infty}^{\infty} \sum_{l=-\infty}^{\infty} g(n - 2k)h(m - 2l)D_{2^j,2}^d f(k,l)$$
$$+ 2 \sum_{k=-\infty}^{\infty} \sum_{l=-\infty}^{\infty} g(n - 2k)g(m - 2l)D_{2^j,3}^d f(k,l).$$
$$(12)$$

Therefore, in order to recover the approximation at level $j+1$, the approximations at level j are filtered by $h(m)h(n)$, and the detail coefficients are filtered by $h(n)g(m)$, $g(n)h(m)$, and $g(n)g(m)$, respectively. These wavelet reconstruction filters in the Fourier domain are given by

$$H_r^A(\omega_1, \omega_2) = H(\omega_1)H(\omega_2)$$
$$H_r^{D^1}(\omega_1, \omega_2) = H(\omega_1)G(\omega_2)$$
$$H_r^{D^2}(\omega_1, \omega_2) = G(\omega_1)H(\omega_2)$$
$$H_r^{D^3}(\omega_1, \omega_2) = G(\omega_1)G(\omega_2). \quad (13)$$

Fig. 1(b) shows the block diagram of the analysis filter bank which obtains the approximation at level j from the approximations and detail at level $j - 1$. This block diagram can be used in a pyramidal structure to reconstruct $A_1^d f$, the approximation at resolution 1, from the set $(A_{2^J}^d f, D_{2^j}^d f)_{-J \leq j \leq -1}$. In those applications that we are interested in namely recovering a local region of the image from the approximate and detail coefficients, we have to calculate these coefficients for that region plus a margin for the support of the wavelet reconstruction filters. That margin is equal to half of the length of the filters h and g.

C. Wavelet Reconstruction from the Projection Data

In this section, we present an algorithm that can be used to obtain the wavelet coefficients of a function on R^2 from its Radon transform data. In those applications for which one is interested in the wavelet coefficients of the function, it involves fewer computations than first reconstructing the function and then taking its wavelet transform. Also using this method, one can obtain locally the wavelet coefficients of a function, which will allow the local reconstruction of a function and can be used in local tomography. This property will be explained in Section IV. We first introduce the main formulas for the reconstruction of the continuous wavelet transform directly from the Radon transform data.

Given a real-valued, square integrable function g on R^2 that satisfies condition (6), let f be given on R^2, the wavelet transform of function f can be reconstructed from its 1-D projections by

$$W_u^{(2)}(g; f)(\vec{v}) = f * \tilde{g}_u(u\vec{v})$$
$$= u^{1/2} \int_0^{\pi} (H\partial R_\theta \tilde{g}_u * R_\theta f)$$
$$\cdot ((u^{-1}x)\cos\theta + (u^{-1}y)\sin\theta) \, d\theta \quad (14)$$

where $\vec{v} = [x \ \ y] \in R^2$. In the discrete case the above equation becomes

$$W_{2^j}^{(2)}(g; f)(\vec{n}) = \int_0^{\pi} (H\partial R_\theta \tilde{g}_{2^j} * R_\theta f)$$
$$\cdot ((2^{-j}n_1)\cos\theta + (2^{-j}n_2)\sin\theta) \, d\theta \quad (15)$$

SCALING FUNCTION

MOTHER WAVELET

(a)

(b)

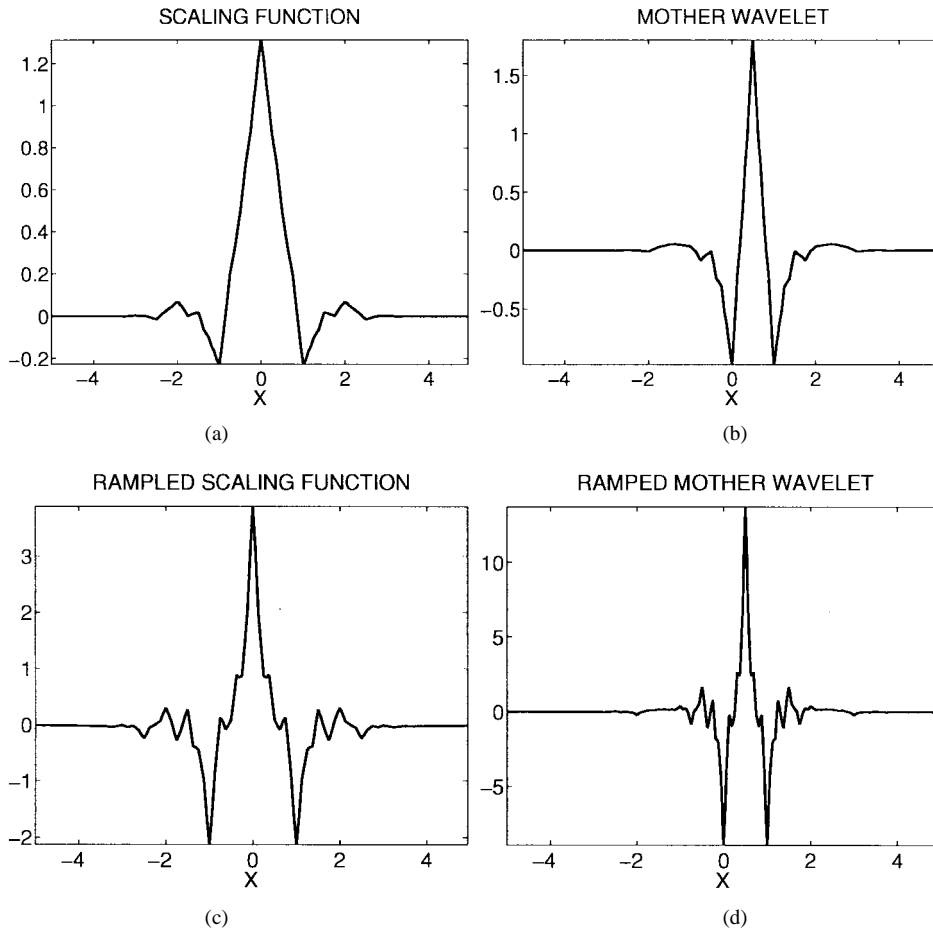RAMPLED SCALING FUNCTION

RAMPED MOTHER WAVELET

(c)

(d)

Fig. 3. Wavelet with less dissimilar lengths, $l = k = \bar{k} = 4$. (a) Scaling function. (b) Wavelet basis. (c) Ramp-filtered scaling function. (d) Ramp-filtered wavelet basis.

where $\vec{n} = [n_1 \quad n_2]$. The right-hand side can be evaluated in two steps, the filtering step,

$$Q_{2^j,\theta}(t) = (R_\theta f * H\partial R_\theta \tilde{g}_{2^j})(2^{-j}t)$$

and the backprojection step

$$W_{2^j}^{(2)}(g;f)(\vec{n}) = \int_0^\pi Q_{2^j,\theta}(n_1\cos\theta + n_2\sin\theta)\, d\theta. \quad (16)$$

The filtering step can be implemented in Fourier domain as

$$\hat{Q}_{2^j,\theta}(\omega) = \widehat{R_\theta f}(\omega)|\omega|\hat{\tilde{g}}_{2^j}(\omega\cos\theta, \omega\sin\theta)W(\omega)$$

where $\hat{\tilde{g}}_{2^j}(\omega_1,\omega_2), \hat{Q}_{2^j,\theta}(\omega)$ and $\widehat{R_\theta f}(\omega)$ are the Fourier transforms of the functions $\tilde{g}_{2^j}, Q_{2^j,\theta}$ and $R_\theta f$, respectively, and $W(\omega)$ is a smoothing window. Therefore, (15) can be implemented using the same algorithm as the conventional filtered backprojection method while the ramp filter $|\omega|$ is replaced by the wavelet ramp filter $|\omega|\hat{\tilde{g}}_{2^j}(\omega\cos\theta, \omega\sin\theta)$.

If the wavelet basis is separable, the approximation and detail coefficients are given by (9) and (11). These coefficients can be obtained from the projection data by (15), replacing $g(\vec{v})$ by $\Phi(x,y) = \phi(x)\phi(x), \Psi^1(x,y) = \phi(x)\psi(x), \Psi^2(x,y) = \psi(x)\phi(x)$, and $\Psi^3(x,y) = \psi(x)\psi(x)$, respectively. For example, the approximation coefficients are

obtained by

$$A_{2^j}^d f(n,m) = W_{2^j}^{(2)}(\Phi; f)([n \quad m])$$
$$= 2^{j/2}\int_0^\pi (H\partial R_\theta \tilde{\Phi}_{2^j} * R_\theta f)$$
$$\cdot ((2^{-j}n)\cos\theta + (2^{-j}m)\sin\theta)\, d\theta. \quad (17)$$

These coefficients can be calculated using the standard filtered backprojection method, while the filtering part in the Fourier domain is given by

$$\hat{Q}_{A_{2^j}^d,\theta}(\omega) = \hat{R}_\theta f(\omega)|\omega|\hat{\tilde{\Phi}}_{2^j}(\omega\cos\theta, \omega\sin\theta)W(\omega)$$

where $\hat{\tilde{\Phi}}_{2^j}(\omega\cos\theta, \omega\sin\theta) = \hat{\tilde{\phi}}_{2^j}(\omega\cos\theta)\hat{\tilde{\phi}}_{2^j}(\omega\sin\theta)$. The detail coefficients can be found in a similar way as

$$D_{2^j,i}^d f = W_{2^j}^{(2)}(\Psi^i; f)([n \quad m]) \quad \text{for} \quad i = 1,2,3. \quad (18)$$

To get the detail coefficients, the filtering step is modified as

$$\hat{Q}_{D_{2^j,i}^d,\theta}(\omega) = \hat{R}_\theta f(\omega)|\omega|\hat{\tilde{\Psi}}_{2^j}^i(\omega\cos\theta, \omega\sin\theta)W(\omega)$$

$$\text{for} \quad i = 1,2,3.$$

This means that the wavelet and scaling coefficients of the image can be obtained by filtered backprojection method while
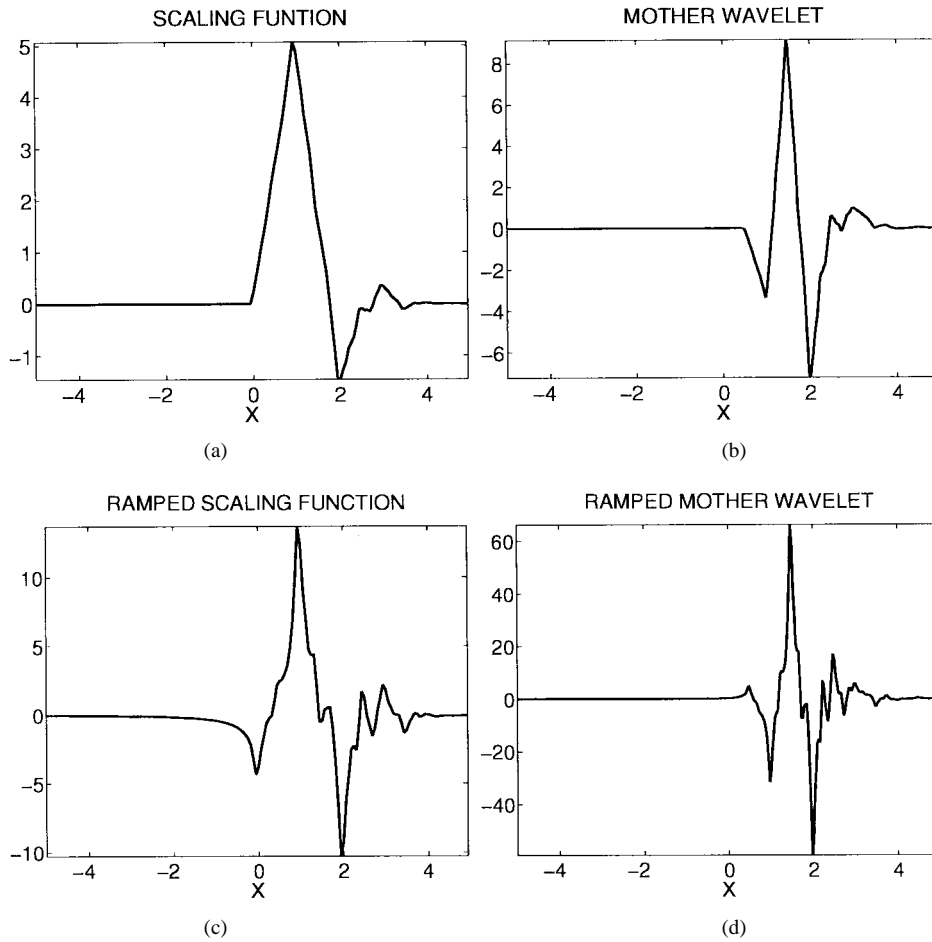
Fig. 4.   Wavelet with extremal phase and highest number of vanishing moments with length 4. (a) Scaling function. (b) Wavelet basis. (c) Ramp-filtered scaling function. (d) Ramp-filtered wavelet basis.

the ramp filter is replaced by

$$
\begin{aligned}
H_\theta^A &= |\omega| \hat{\hat{\Phi}}_{2^j}(\omega \cos\theta, \omega \sin\theta) \\
&= |\omega| \hat{\hat{\phi}}_{2^j}(\omega \cos\theta) \hat{\hat{\phi}}_{2^j}(\omega \sin\theta) \\
H_\theta^{D^1} &= |\omega| \hat{\hat{\Psi}}_{2^j}^1(\omega \cos\theta, \omega \sin\theta) \\
&= |\omega| \hat{\hat{\phi}}_{2^j}(\omega \cos\theta) \hat{\hat{\psi}}_{2^j}(\omega \sin\theta) \\
H_\theta^{D^1} &= |\omega| \hat{\hat{\Psi}}_{2^j}^2(\omega \cos\theta, \omega \sin\theta) \\
&= |\omega| \hat{\hat{\psi}}_{2^j}(\omega \cos\theta) \hat{\hat{\phi}}_{2^j}(\omega \sin\theta) \\
H_\theta^{D^1} &= |\omega| \hat{\hat{\Psi}}_{2^j}^3(\omega \cos\theta, \omega \sin\theta) \\
&= |\omega| \hat{\hat{\psi}}_{2^j}(\omega \cos\theta) \hat{\hat{\psi}}_{2^j}(\omega \sin\theta)
\end{aligned} \tag{19}
$$

which are called the scaling and wavelet ramp filters. In order to obtain pyramidal wavelet coefficients, the $A_{2^j}^d f$ and $D_{2^j,i}^d f, i = 1, 2, 3, -J \leq j \leq -1$ are found using (18) and (17). To reconstruct the image from these coefficients, we use the multiresolution reconstruction formulas (12). Fig. 2 shows the block diagram of the multiresolution reconstruction system. The reconstruction part uses the conventional multiresolution reconstruction filterbank (cf. Fig. 1), which appear as black boxes in the block diagram.

IV. LOCAL RECONSTRUCTION

It has been noted [2], [8] that if a function has a large number of vanishing moments (or, equivalently, if its Fourier transform vanishes to high order at the origin), then its Hilbert transform will decay very rapidly at infinity. If a compactly supported function has this property, then the essential support of its Hilbert transform (5) should not be large. This phenomenon is in part a manifestation of the observation made in [20] that an integral operator with singular kernel of Calderon–Zygmund type is almost diagonalized in a wavelet basis.

More specifically, the following holds.

Lemma 1: Suppose that $f(t) = 0$ outside the interval $[-A, A]$ and satisfies $\int t^n f(t)\, dt = 0$ for $n = 0, 1, \cdots, N$. Then for $|s| > A$,

$$
|Hf(s)| \leq \frac{1}{\pi |s - A|^{N+2}} \int_{-A}^A |f(t) t^{N+1}|\, dt.
$$

Proof: Assume that $s > A$. The argument for $s < -A$ is the same. Since

$$
Hf(s) = \lim_{\epsilon \to 0} \frac{1}{\pi} \int_{|t| > \epsilon} \frac{f(s - t)}{t}\, dt
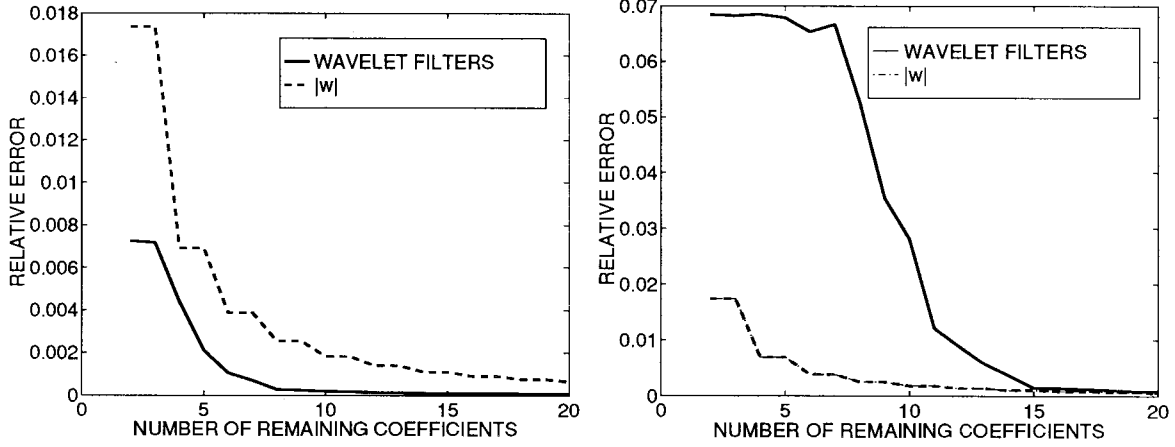$$

Fig. 5. Normalized error (23) versus the number of remaining coefficients. (a) Biorthogonal wavelet with less dissimilar lengths ([15, Tab. III]). (b) Orthogonal wavelet with external phase and highest number of vanishing moments with length 4 ([16, Tab. 6.2]).

since $f(t) = 0$ outside $[-A, A]$, and since $s > A$

$$Hf(s) = \frac{1}{\pi} \int_{s-A}^{s+A} \frac{f(s-t)}{t} \, dt.$$

Fixing s, and expanding $1/t$ in a Taylor series about $t = s$ gives for some $t_s \in [s - A, s + A]$

$$\begin{aligned} Hf(s) &= \frac{1}{\pi} \int_{s-A}^{s+A} f(s-t) \left[\sum_{k=0}^{N} \frac{(s-t)^k}{s^{k+1}} + \frac{(s-t)^{N+1}}{t_s^{N+2}} \right] dt \\ &= \frac{1}{\pi} \sum_{k=0}^{N} \frac{1}{s^{k+1}} \int_{-A}^{A} f(t) t^k \, dt + \frac{1}{2\pi i} \\ &\quad \cdot \int_{s-A}^{s+A} t_s^{-N-2} f(s-t)(s-t)^{N+1} \, dt \\ &= \frac{1}{\pi} \int_{s-A}^{s+A} t_s^{-N-2} f(s-t)(s-t)^{N+1} \, dt \end{aligned}$$

Since $t_s \in [s - A, s + A], |t_s|^{-N-2} \le |s - A|^{-N-2}$, so that

$$|Hf(s)| \le \frac{1}{\pi |s-A|^{N+2}} \int_{-A}^{A} |f(t) t^{N+1}| \, dt.$$

□

The significance of this observation for local tomography is the following. If $\psi(t)$ is the wavelet corresponding to the scaling function $\varphi(t)$ for a multiresolution analysis, then at least the zeroth moment of ψ must vanish. It is possible to design wavelets that have compact support and have many vanishing moments. In this case, the functions $H\partial R_\theta \Psi^i(t)$, where $\Psi^i, i = 1, 2, 3$ are given by (10), will have very rapid decay for each θ. Numerically, even for wavelets with a few vanishing moments, the essential support of $H\partial R_\theta \Psi^i(t)$ is the same as the support of $R_\theta \Psi^i(t)$ for each θ. This means that by (14), the discrete wavelet coefficients (18) can be computed locally using essentially local projections.

Rapid decay after ramp filtering is also observed in scaling functions $\varphi(t)$ provided that φ has vanishing moments. Specifically, if $\varphi(t)$ satisfies $\int \varphi(t) \, dt = 1$ and $\int t^j \varphi(t) \, dt = 0$ for $j = 1, 2, \cdots, N$, then $\partial \varphi$ satisfies $\int \varphi(t) \, dt = 0, \int t \varphi(t) \, dt =$
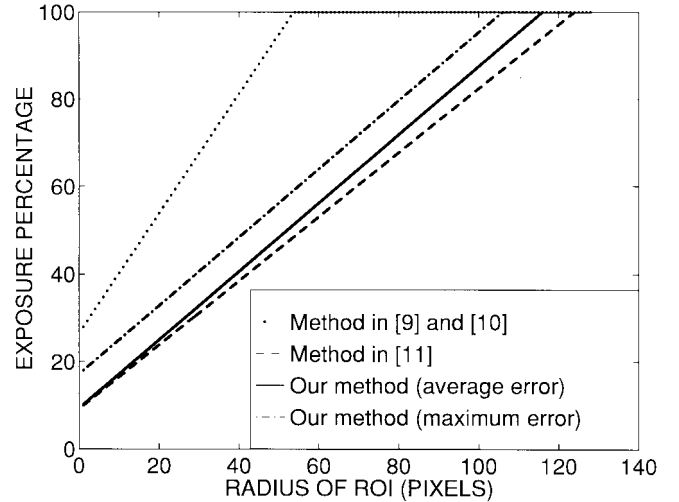

Fig. 6. Exposure percentage versus the size of the ROI.

1, and $\int t^j \varphi(t) \, dt = 0$ for $j = 2, 3, \cdots, N + 1$. Therefore, as in Lemma 1, it follows that

$$|H\partial \varphi(s)| \le \frac{1}{\pi s^2} + \frac{1}{\pi |s-A|^{N+3}} \int |\partial \varphi(t) t^{N+2}| \, dt.$$

Even though the decay is dominated by the s^{-2} term, ramp-filtered scaling functions with vanishing moments display significantly less relative energy leakage outside the support of the scaling function than those without vanishing moments.

In order to quantify this locality phenomenon, we define the *spread* of a function f with respect to an interval I under ramp-filtering to be the normalized energy of the function $(|\omega| \hat{f}(\omega))^\vee(t)$ outside I, i.e., with $\overline{I}$ denoting the complement of I

$$\text{spread}(f; I) = \left(\int_{\overline{I}} |(|\omega| \hat{f}(\omega))^\vee(t)|^2 \, dt \right)^{1/2} \bigg/ \left(\int_{-\infty}^{\infty} |(|\omega| \cdot \hat{f}(\omega))^\vee(t)|^2 \, dt \right)^{1/2}.$$

The rapid decay of the ramp-filtered scaling functions is related to the number of vanishing moments of the scaling
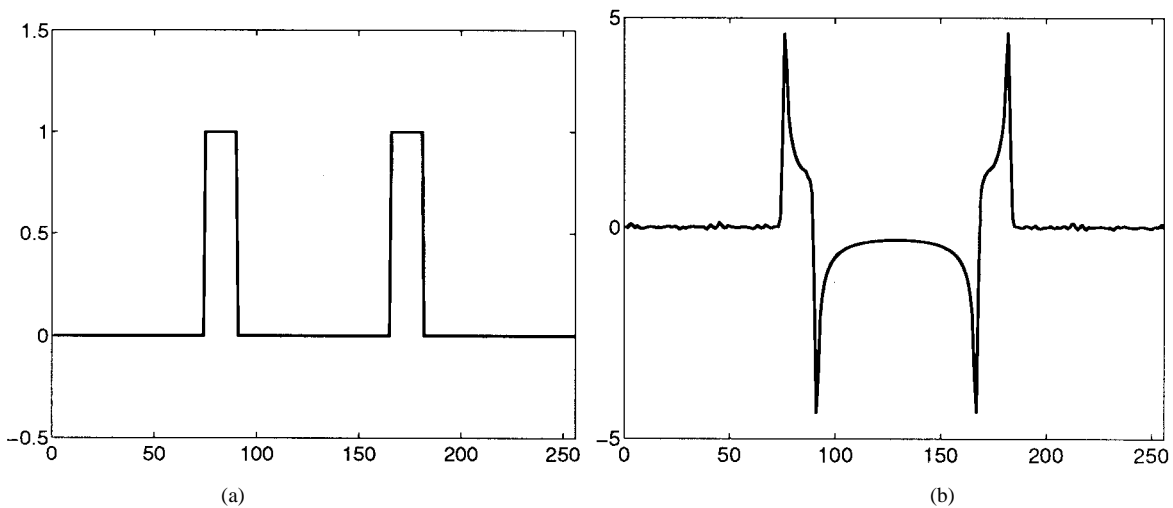
Fig. 7.   (a) Projection of a null-space element. (b) Reconstruction of the null-space element.

function. Orthonormal wavelets corresponding to scaling functions with vanishing moments have been called "coiflets" by Daubechies in [6, Sec. 8.2]. For coiflets with 1 and 3 vanishing moments, supported on the intervals [0, 5], and [0, 11], respectively, we have measured spreads with respect to these intervals of .016 and .013, respectively. These scaling functions correspond to scaling filters with 6 and 12 taps, respectively. Daubechies has also observed in [6, Sec. 8.3.5], that the symmetric biorthogonal bases constructed in [15] are numerically very close to coiflets. For the biorthogonal "near-coiflet" scaling functions supported on the intervals [0, 4], [0, 8], and [0, 12], we have measured spreads with respect to these intervals of .029, .016, and .0095, respectively. These scaling functions correspond to scaling filters with 5, 9, and 13 taps, respectively. For the purposes of this paper, it is most desirable to minimize both the spread of the scaling function and the number of taps in the corresponding filter. Under these criteria, the near-coiflet filter with 5 taps is near optimal [see Fig. 3(a) and (c) and Fig. 5(a)] and is therefore used in our simulations. The measured spreads for various compactly supported wavelet and scaling functions are given in

Table I. We have observed that even if g is replaced by scaling function given by (8), $H\partial R_\theta g$ has essentially the same support as $R_\theta g$ for each θ. Fig. 3 shows the Daubechies' biorthogonal wavelet and scaling function ([15, Table III]) as well as the ramp filtered version of these functions. Observe that the ramp-filtered scaling functions has almost the same essential support as the scaling function itself.[1] Therefore, in order to reconstruct the wavelet and scaling coefficients for some wavelet basis, we only need the projections passing through the region of interest plus a margin for the support of the wavelet and scaling ramp filters. Moreover, in order to reconstruct the image from the wavelet and scaling coefficients, we have to calculate these coefficients in the ROI plus a margin for the support of the wavelet reconstruction filters (13). Since wavelet and scaling

---

[1] This is not the case in general, for example, in Fig. 4 we have plotted another wavelet and scaling functions ([16, Tab. 6.2]) and their ramp-filtered versions, for comparison. The scaling function in this basis does spread significantly after ramp filtering.
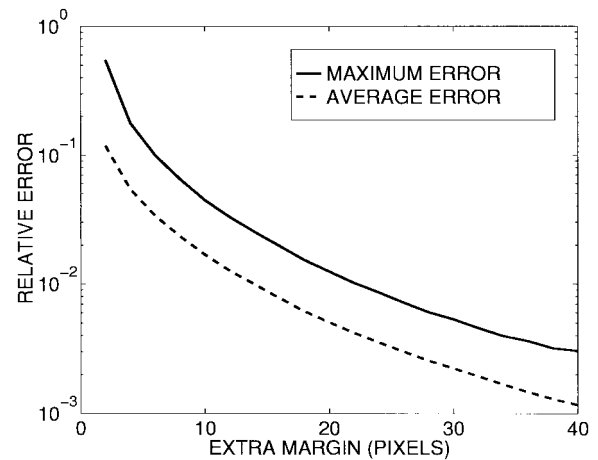

Fig. 8.   Maximum error and average error versus the amount of nonlocal data used in the reconstruction scheme.

ramp filters and also the wavelet reconstruction filters get wider in lower scales, we need to increase the exposure to reconstruct the low resolution coefficients in the ROI. In our algorithm, we can reconstruct the scaling coefficients locally, and we use only one level of the wavelet filterbank.

A. Error Analysis

It is mentioned in [23] that the error in the interior Radon transform is not negligible because the derivative Hilbert transform (the impulse response of the filter $|\omega|$) is not local in space. This means that in order to reconstruct even a small local ROI we have to consider some data outside the region of interest to get negligible reconstruction error. We will find an upper bound for the reconstruction error, in terms of the amount of nonlocal data that we consider in the reconstruction. We will also compare the upper bound of the error in a locally reconstructed image using our algorithm to the upper bound of the error when we use the standard filtered backprojection method with local data. For simplicity of notation, we assume the ROI and region of exposure (ROE) are centered at the center of the image. Consider the filtered backprojection

TABLE I
SPREAD OF WAVELET AND SCALING FUNCTIONS

Filter	Coefficients	Support	Wavelet Spread	Scaling Spread
Haar	1 1	[0,1]	.3837	.6900
Linear spline	0.50000000000000 1.00000000000000 0.50000000000000	[0,2]	0.09167	0.3726
Quadratic spline	0.25000000000000 0.75000000000000 0.75000000000000 0.50000000000000 0.25000000000000	[0,3]	0.01691	0.1959
Cubic spline	0.12500000000000 0.50000000000000 0.75000000000000 0.50000000000000 0.12500000000000	[0,4]	0.003767	0.1389
Degree 4 spline	0.06250000000000 0.31250000000000 0.62500000000000 0.62500000000000 0.31250000000000 0.06250000000000	[0,5]	0.0009341	0.1105
Daubechies 4 tap filter	0.68301270189222 1.18301270189222 0.31698729810778 −0.18301270189222	[0,3]	0.03391	0.3449
Daubechies 6 tap filter	0.47046720778416 1.14111691583144 0.65036500052623 −0.19093441556833 −0.12083220831040 0.04981749973688	[0,5]	0.005446	0.1929
Daubechies 8 tap filter	0.32580342805100 1.01094571509000 0.89220013842700 −0.03957026356000 −0.26450716736900 0.04650360107100 −0.01498698933040	[0,7]	0.001058	0.1232
Daubechies 10 tap filter	0.22641898258329 0.85394354270476 1.02432694425952 0.19576696134736 −0.34265671538239 −0.04560113188406 0.10970265864207 −0.00882680010864 −0.01779187010184 0.00471742793840	[0,9]	0.0002376	0.08907
Coiflet with 1 moment vanishing	−0.05142972847100 0.23892972847100 0.60285945694200 0.27214054305800 −0.05142997284700 −0.01107027152900	[0,5]	0.0003069	0.01613

formula (1), while the ramp filter $|w|$ is replaced by a general angle dependent filter $h_\theta(s)$

$$f_r(x,y) = \int_0^\pi (h_\theta(s) * R_\theta f(s))(x\cos\theta + y\sin\theta)\,d\theta. \quad (20)$$

We assume that for each angle $\theta \in [0, 2\pi)$, the projection data $R_\theta f(s)$ is sampled with a radial sampling interval of T_s, and the support of f is a disk of radius R centered at the origin. The region of interest, a disc of radius r_i pixels centered at the origin, will be denoted by ROI, and the region of exposure, a disc of radius r_e pixels centered at the origin,

will be denoted by ROE. If $h_\theta(s)$ is chosen to be the impulse response of the ramp filter (2), the reconstructed function $f_r(x,y)$ is an approximation of the function f; and if it is the impulse response of the wavelet and scaling ramp filters (19), the reconstructed function $f_r(x,y)$ will be the approximation of the wavelet and scaling coefficients. The discrete version of (20) is given by

$$f_r(x,y) = \frac{\pi}{K} \sum_{k=1}^K \frac{1}{R} \sum_{n=-R}^R P_{\theta_k}(n) h_{\theta_k}(m-n)$$

TABLE I
SPREAD OF WAVELET AND SCALING FUNCTIONS (*continued.*)

Filter	Coefficients	Support	Wavelet Spread	Scaling Spread
Coiflet with 3 moments vanishing	0.01158759673900 −0.02932013798000 −0.04763959031000 0.27302104653500 0.57468239385700 0.29486719369600 −0.05408560709200 −0.04202648046100 0.01674441016300 0.00128920335600 −0.00050950539900	[0,11]	0.000006154	0.01307
Near coiflet (5 taps)	−0.05000000000000 0.25000000000000 0.60000000000000 0.25000000000000 −0.05000000000000	[0,4]	0.001682	0.02890
Near coiflet (9 taps)	0.01250000000000 −0.03125000000000 −0.05000000000000 0.28125000000000 0.57500000000000 0.28125000000000 −0.05000000000000 −0.03125000000000 0.01250000000000	[0,8]	0.00005151	0.01632
Near coiflet (12 taps)	−0.00317382812500 0.00585937500000 0.01904296875000 −0.04882812500000 0.04760742187500 0.29296875000000 0.56347656250000 0.29296875000000 −0.04760742187500 −0.04882812500000 0.01904296875000 0.00585937500000 −0.00317382812500	[0,12]	0.000001515	0.009547

where $m = \lfloor (x\cos\theta + y\sin\theta)/T_s \rfloor \in ROE, K$ is the total number of evenly spaced angles at which the projections are measured, $P_{\theta_k}(n)$ is the projection $R_{\theta_k} f(n/T_s)$, and $\theta_k = k(\pi/K)$. We can divide the inner summation into two parts, corresponding to the ROE and its complement $\overline{ROE}$

$$
f_r(x,y) = \frac{\pi}{K} \sum_{k=1}^{K} \frac{1}{R} \sum_{|n| \le r_e} P_{\theta_k}(n) h_{\theta_k}(m-n)
$$
$$
+ \frac{\pi}{K} \sum_{k=1}^{K} \frac{1}{R} \sum_{|n| > r_e} P_{\theta_k}(n) h_{\theta_k}(m-n).
$$

Thus, the magnitude of error using only ROE is given by

$$
|e(x,y)| = \left| \frac{\pi}{K} \sum_{k=1}^{K} \frac{1}{R} \sum_{|n| > r_e} P_{\theta_k}(n) h_{\theta_k}(m-n) \right|.
$$

To get an upper bound for the error we use the

Cauchy–Schwartz inequality as

$$
|e(x,y)| = \left| \frac{\pi}{K} \sum_{k=1}^{K} \frac{1}{R} \sum_{|n| > r_e} P_{\theta_k}(n) h_{\theta_k}(m-n) \right|
$$
$$
\le \frac{\pi}{K} \sum_{k=1}^{K} \frac{1}{R} \sum_{|n| > r_e} |P_{\theta_k}(n) h_{\theta_k}(m-n)|
$$
$$
\le \frac{\pi}{K} \sum_{k=1}^{K} \frac{1}{R} \left(\sum_{|n| > r_e} |P_{\theta_k}(n)|^2 \right)^{1/2}
$$
$$
\cdot \left(\sum_{|n| > r_e} |h_{\theta_k}(m-n)|^2 \right)^{1/2}.
$$

If we assume that the support of $f(x,y)$ is in the disc of radius 1, then $|P_{\theta_k}(n)| \le 2 \max |f(x,y)|$. Hence

$$
|e(x,y)| \le \frac{2\sqrt{2}\pi}{K} \max |f(x,y)| \frac{\sqrt{R-r_e}}{R}
$$
$$
\cdot \sum_{k=1}^{K} \left(\sum_{|n| > r_e} |h_{\theta_k}(m-n)|^2 \right)^{1/2}.
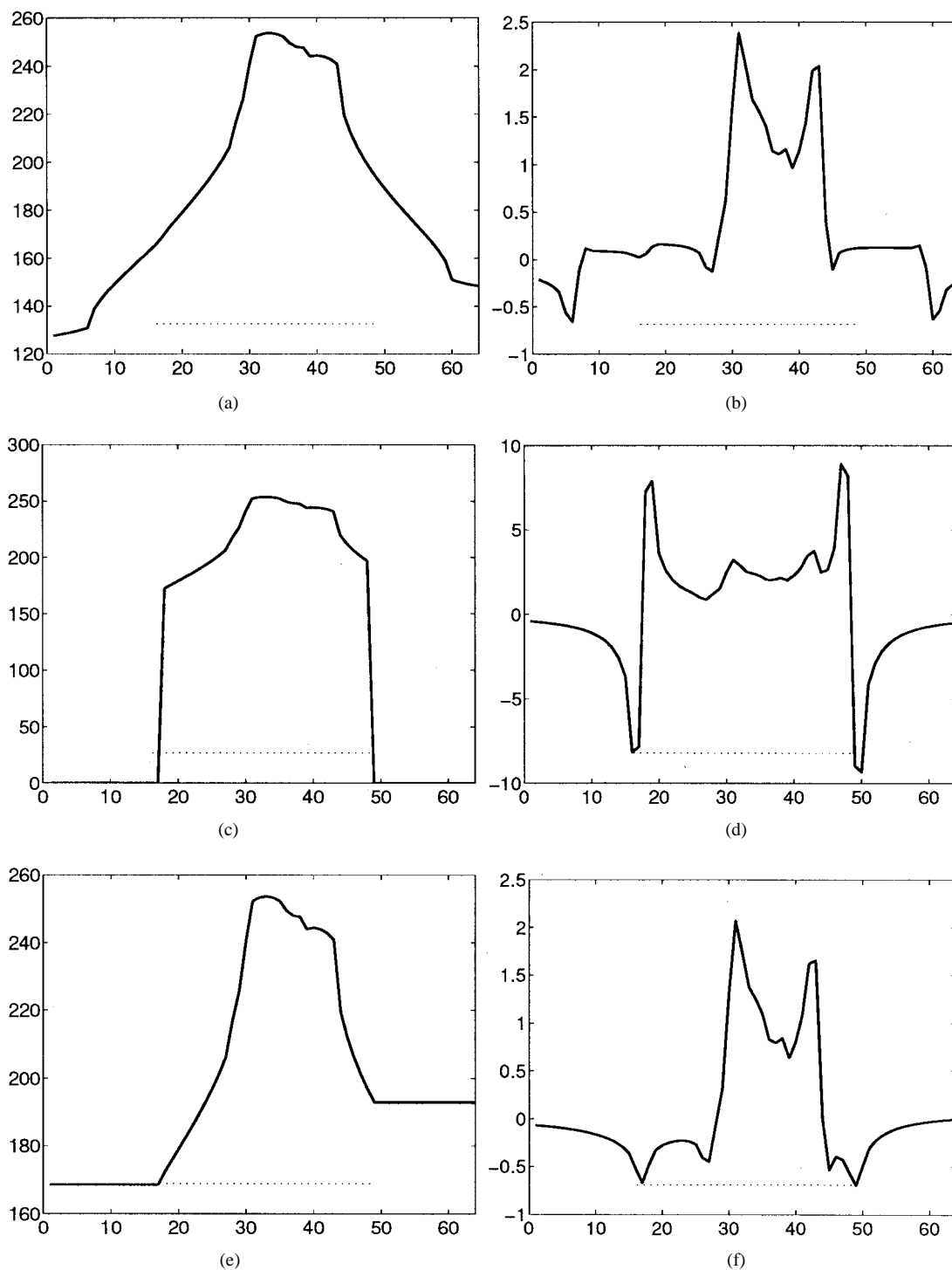$$

Fig. 9. (a) A sample projection with the Shepp–Logan head phantom. (b) Projection filtered by $|\omega|$. (c) Projection when nonlocal data is set to zero. (d) Filtered projection. (e) Projection extrapolated outside the ROI. (f) Filtered projection. (The marked area is the ROE.)

We define the relative error as $|e_{\mathrm{rel}}(x,y)| = |e(x,y)|/\max|f(x,y)|$, then

$$|e_{\mathrm{rel}}(x,y)| \leq \frac{2\sqrt{2}\pi}{K} \frac{\sqrt{R-r_e}}{R}$$
$$\cdot \sum_{k=1}^{K} \left(\sum_{|n|>r_e} |h_{\theta_k}(m-n)|^2 \right)^{1/2}. \quad (21)$$

In the worst case, the ROI is a single point. Thus we may bound (21) by

$$|e_{\mathrm{rel}}(x,y)| \leq \frac{2\sqrt{2}\pi}{K} \frac{\sqrt{R-r_e}}{R} \sum_{k=1}^{K} \left(\sum_{|n|\geq r_e-r_i} |h_{\theta_k}(n)|^2 \right)^{1/2}.$$

We define $h_{\theta_k}^T$, the truncated filter, as

$$h_{\theta_k}^T(n) = \begin{cases} h_{\theta_k}(n) & |n| < r_e - r_i \\ 0 & \text{otherwise.} \end{cases}$$

Therefore

$$|e_{\text{rel}}(x,y)| \leq \frac{2\sqrt{2}\pi}{K} \frac{\sqrt{R-r_e}}{R}$$
$$\cdot \sum_{k=1}^{K} \left(\sum_{n=-R}^{R} |h_{\theta_k}(n) - h_{\theta_k}^T(n)|^2 \right)^{1/2}.$$

The inner sum can be written in the frequency domain. That is

$$|e_{\text{rel}}(x,y)| \leq \frac{2\sqrt{2}\pi}{K} \frac{\sqrt{R-r_e}}{R}$$
$$\cdot \sum_{k=1}^{K} \left(\sum_{l=-R}^{R} |H_{\theta_k}(l) - H_{\theta_k}^T(l)|^2 \right)^{1/2} \qquad (22)$$

where H_{θ_k} and $H_{\theta_k}^T$ are the Fourier transform of h_{θ_k} and $h_{\theta_k}^T$, respectively. In order to calculate the upper bound of the error in standard filtered backprojection method, we replace h_{θ_k} in (22) by the ramp filter (2). The upper bound for the error in the reconstruction of wavelet and scaling coefficients can be obtained by replacing H_{θ_k} in (22) with (19). In our algorithm, the scaling and wavelet coefficients at resolution 2^{-1} are reconstructed directly from the projection data. The recovered coefficients are then filtered by the reconstruction filters (13) to obtain the original image. To consider the effect of the wavelet reconstruction filterbank in the error upper bound, we move these filters to the projection domain, i.e.,

$$|e_{\text{rel}}(x,y)|$$
$$\leq \frac{2\sqrt{2}\pi}{K} \frac{\sqrt{R-r_e}}{R} \sum_{k=1}^{K} \left(\sum_{l=-R}^{R} |E_{\theta_k}^A(l)|^2 \right)^{1/2}$$
$$+ \left(\sum_{l=-R}^{R} |E_{\theta_k}^{D^1}(l)|^2 \right)^{1/2} + \left(\sum_{l=-R}^{R} |E_{\theta_k}^{D^2}(l)|^2 \right)^{1/2}$$
$$+ \left(\sum_{l=-R}^{R} |E_{\theta_k}^{D^3}(l)|^2 \right)^{1/2} \qquad (23)$$

where

$$E_{\theta_k}^A(l) = F_{\theta_k}^A(l) - F_{\theta_k}^{A^T}(l)$$
$$E_{\theta_k}^{D^i}(l) = F_{\theta_k}^{D^i}(l) - F_{\theta_k}^{D^{i^T}}(l), \qquad i = 1, 2, 3$$

where $F_{\theta_k}^A = H_{\theta_k}^A H_r^A(l\cos\theta, l\sin\theta)$ and $F_{\theta_k}^{D^i} = H_{\theta_k}^{D^i} H_r^{D^i}(l\cos\theta, l\sin\theta)$, with $H_{\theta_k}^A, H_{\theta_k}^{D^1}, H_{\theta_k}^{D^2}$ and $H_{\theta_k}^{D^3}$ being the ramped scaling and wavelet filters (19), $H_r^A, H_r^{D^1}, H_r^{D^2}$, and $H_r^{D^3}$ the wavelet reconstruction filters (13), and $F_{\theta_k}^{A^T}, F_{\theta_k}^{D^{i^T}}, i = 1, 2, 3$ the truncated versions of the filters $F_{\theta_k}^A$ and $F_{\theta_k}^{D^i}, i = 1, 2, 3$. The normalized upper bound of the relative error in the reconstructed image, versus the amount of nonlocal data $(r_e - r_i)$ is depicted in Fig. 5. These bounds are given by (22) and (23) for the standard filtered backprojection method and our algorithm, respectively. The horizontal axis in Fig. 5 shows the amount of nonlocal data that is collected in order to reconstruct the ROI.

B. Interior Problem

The interior problem in even dimensions is not uniquely solvable, since there are nonzero functions that have zero projections on the ROE. Clearly, our algorithm will be unable to reconstruct such a function. It has been noted that these functions, which are in the null-space of the interior problem, do not vary much well inside the ROE [23].

To illustrate this, we will reconstruct an element of the null-space and measure the variation of this element on the ROI. We assume that the ROI is the interior 32 pixels of the image and ROE is the ROI plus a margin of 22 pixels in each side. This margin shows the amount of nonlocal data used in the reconstruction scheme. Fig. 7(b) shows a slice of a circularly symmetric element of the null-space. The projection of this element for each angle is shown in Fig. 7(a) . The projections are zero inside the ROE, which is the interior 76 pixels of the projections, and one in 16 pixels at each side of the ROE. The measured maximum variation of the null-space on the ROI is less than 1%. We consider two measure criteria for the error in the local reconstruction: the maximum error and the average error. Since, in our approach, most of the error occurs in a small ring at the boundary of the ROI, the average error is an order of magnitude smaller than the maximum error. The maximum error and the average error of the null-space element on the ROI versus the amount of nonlocal data (the difference of the radius of the ROE and ROI) is shown in Fig. 8. Based on the upper limit on the average error or maximum error, we determine the size of extra margin to collect the nonlocal data. In order to limit the maximum error to 1%, we require a margin of 22 pixels, and in order to limit the average error to 1%, we require a margin of 12 pixels.

In Section V, we will present a method to reduce the error at the boundaries of the ROI. In consequence, the amount of error is much smaller than the upper bound predicted by the null space element energy in the ROI. In Section VI, we will show that the reconstruction of the ROI using only 12 pixels of extra margin results in a reconstruction with negligible error in the ROI.

In the sequel, we calculate the amount of exposure versus the size of ROI in our method and previous methods. Let the support of reconstruction filters in the wavelet filterbank be $2r_r$ samples. And also consider an extra margin of $2r_m$ samples in the projection domain, and denote the radius of the region of interest by r_i. The radius of the region of exposure is $r_e = r_i + r_m + r_r$ pixels. The amount of exposure in our algorithm normalized to the full exposure is given by

$$\frac{r_r + r_m + r_i}{R}.$$

The amount of exposure in our algorithm with $r_m + r_r = 12$ pixels and $r_m + r_r = 22$ pixels is plotted in Fig. 6. In the Delaney and Bresler's algorithm [9] the exposure is given by

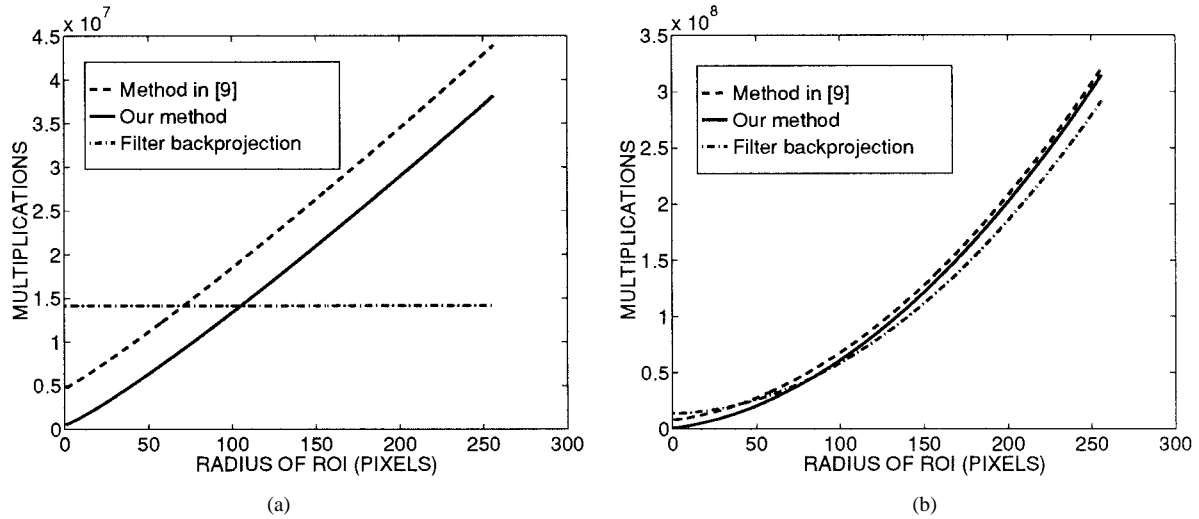$$2^{-L} + \sum_{q=1}^{L} 2^{-q+1} \left(\frac{r_r + r_m + r_i}{R} \right)$$

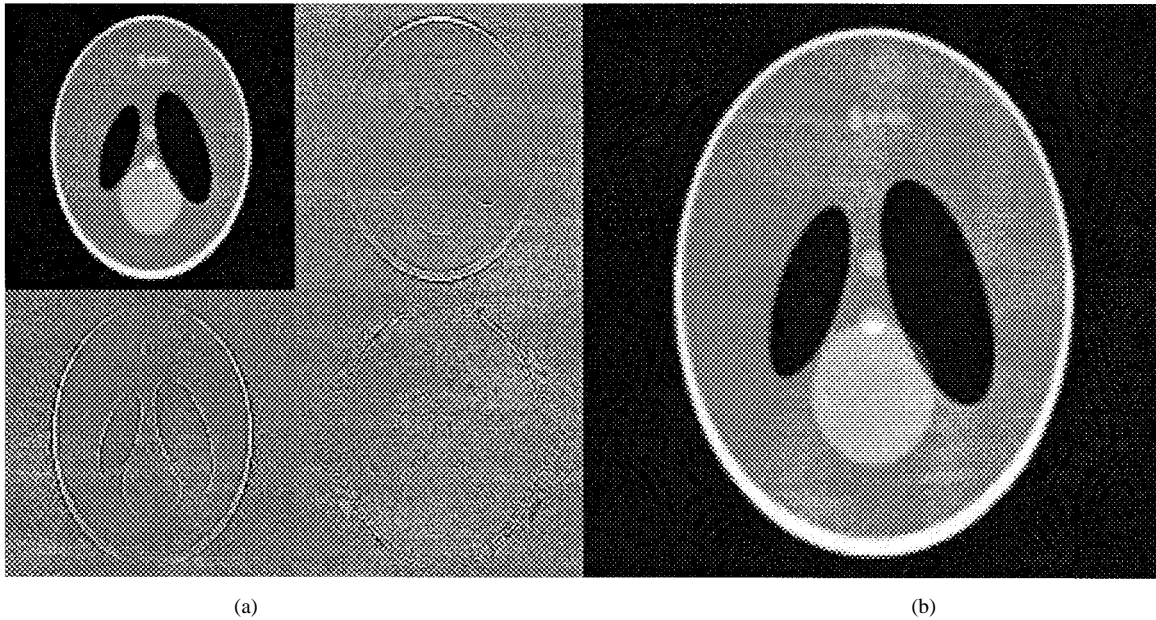Fig. 10.   (a) Complexity of filtering part. (b) Total complexity.

Fig. 11.   (a) Wavelet coefficients. (b) Reconstruction from wavelet coefficients.

where L is the number of levels in the wavelet filterbank. Similar exposure is required in DeStefano and Olson's algorithm [8]. Fig. 6 shows the relative amount of exposure versus the size of the region of interest in a 256×256 image for $r_m + r_r = 12$ pixels for these methods. Also the amount of exposure for [11] is plotted for comparison. All of the exposures in Fig. 6 are divided by two if we use interlaced sampling.

V. IMPLEMENTATION

A. Practical Considerations

In local reconstruction, artifacts are common close to the boundary of the ROE. To illustrate this, we consider the Shepp–Logan head phantom and an ROE of diameter 32 pixels at the center of the image. We set the projections outside the ROE to zero [see Fig. 9(c)] and apply the filtering part of the filtered backprojection formula (2) to the remaining projections. Fig. 9(d) shows the artifacts that appear at the borders of the region of exposure. When the backprojection formula is applied to the filtered projections, these artifacts cause large errors at the borders of the ROE in the reconstructed image.

In order to avoid the artifacts, we have extrapolated the projections continuously to be constant on the missing projections. The extrapolation scheme is the same even when the ROE is not centered. Let the ROE's, which is the subset of projections on which $R_\theta f$ is given, be a circle of radius r_e whose center is located at polar coordinates (r, θ_0), i.e,

$$\text{ROE: } \{s: \ s \in [r\cos(\theta - \theta_0) - r_e, r\cos(\theta - \theta_0) + r_e]\}. \quad (24)$$

(a)   (b)
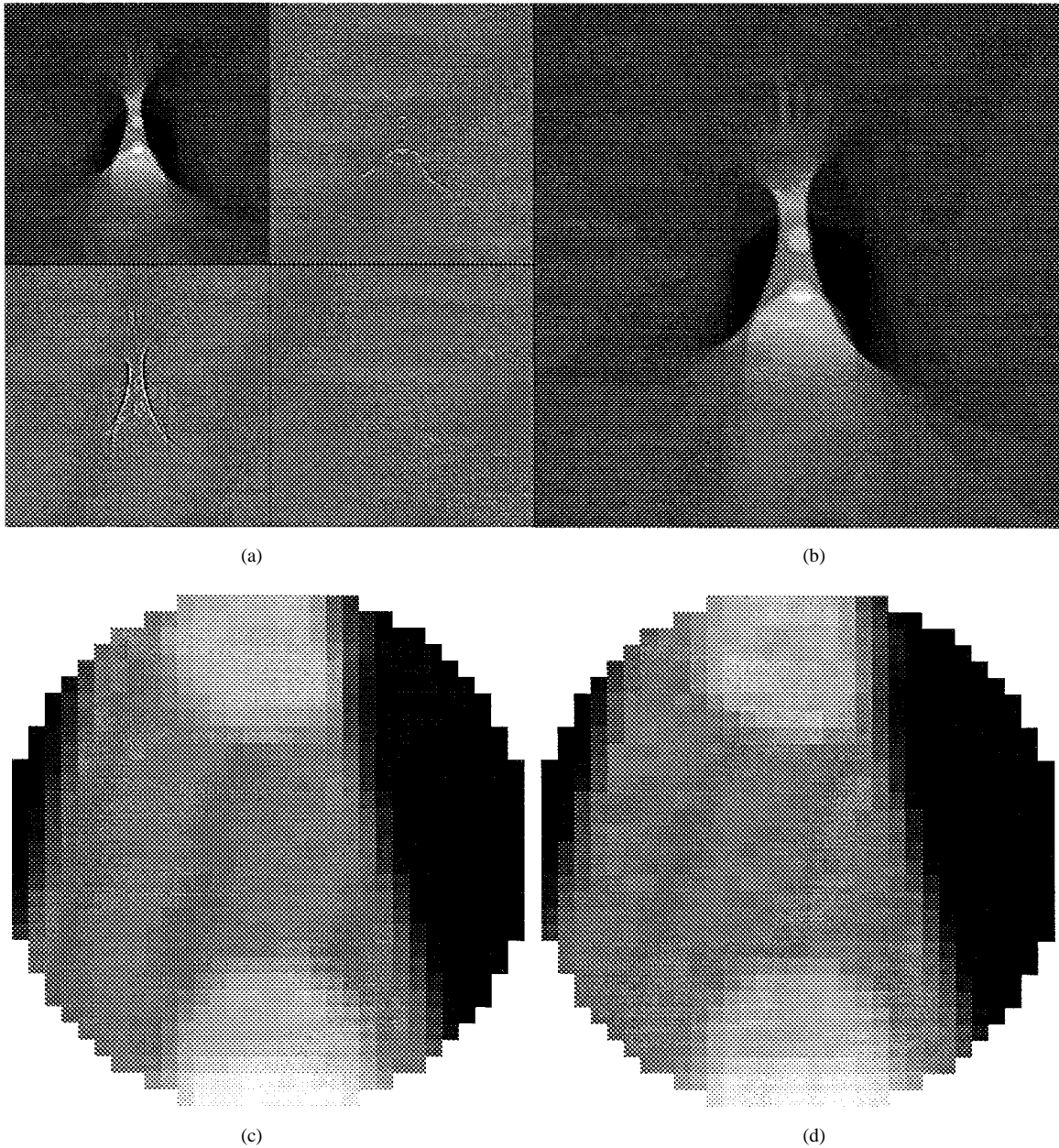
(c)   (d)

Fig. 12. Local wavelet reconstruction. (a) Wavelet coefficients. (b) Reconstruction from wavelet coefficients; blowup of the region of interest. (c) Reconstruction using wavelet method (local data). (d) Reconstruction using standard filtered backprojection method (global data).

We use the constant extrapolation

$$
\begin{aligned}
&(R_\theta)_{\text{local}}(s) \\
&= \begin{cases}
R_\theta(s) & \text{if } s \in \text{ROE} \\
R_\theta(r\cos(\theta - \theta_0) + r_e) & \\
& \text{if } s \in [r\cos(\theta - \theta_0) + r_e, +\infty) \\
R_\theta(r\cos(\theta - \theta_0) - r_e) & \\
& \text{if } s \in (-\infty, r\cos(\theta - \theta_0) - r_e].
\end{cases}
\end{aligned}
\tag{25}
$$

Fig. 9(e) and (f) shows an extrapolated projection and its ramp-filtered version (2), respectively. When we apply the ramp filter to the extrapolated projection, there is no spike at the edge of the region of exposure. The comparison with the ramp-filtered version of the projection using global data [see Fig. 9(b)] shows that the filtered projection has a constant

bias difference compared to the one using global data. This is natural in local tomography and, after backprojection of all projections, appears as a constant bias in the locally reconstructed image [23], [25]. In [23], it is suggested to extrapolate the data outside the ROI using a minimum norm approach, which has the same effect on the artifacts (cf., [23], Fig. VI.8).

B. Algorithm

We assume the support of image is a disc of radius R, and the radius of the ROI is r_i. A region of radius $r_e = r_i + r_m + r_r$ is exposed, where r_m and r_r are the extra margin due to the support of the decomposition filters in the projection domain and the reconstruction filters in the image domain,
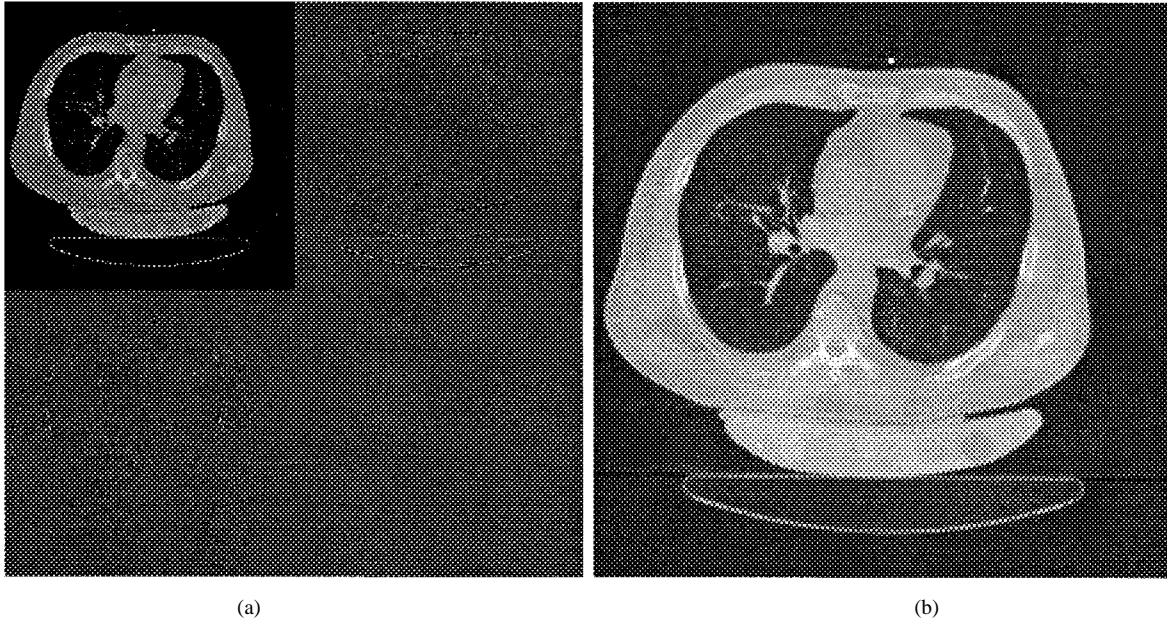
(a)   (b)

Fig. 13.   (a) Wavelet coefficients. (b) Reconstruction from wavelet coefficients.

respectively. Suppose the projections are sampled at N evenly spaced angles. In the following we summarize the algorithm.

1) The region of exposure of each projection is filtered by modified wavelet filters (2), at N angles. The complexity of this part, using FFT, is $\frac{9}{2}Nr_e \log r_e$.

2) The bandwidth of the projections is reduced by half after filtering with modified scaling filters. Hence, we use $N/2$ of the projections at evenly spaced angles. These projections are extrapolated to $4r_e$ pixels, using (25), and are then filtered by modified scaling filters. The complexity of filtering part using the fast Fourier transform (FFT) is $3N(4r_e) \log 4r_e$.

3) Filtered projections are obtained in step 1 and 2 are backprojected to every other point, using (16), to obtain the approximation (17) and detail (18) coefficients at resolution 2^{-1}. The remaining points are set to zero. The complexity of this part, using linear interpolation, is $(7N/2)(r_i + 2r_r)^2$.

4) The image is reconstructed from the wavelet and scaling coefficients by (12). The complexity of filtering is $4(2r_i)^2(3r_r)$.

We have compared the complexity of the filtering part of our algorithm with the filtered backprojection method and the algorithm presented in [9]. Fig. 10(a) shows the complexity of each method as a function of the radius of the region of interest. The complexity of our algorithm and the algorithm proposed in [9] is less than the standard filtered backprojection method when the size of the ROI is small. But as the radius of the ROI is increased, the complexity of both algorithms exceeds that of filtered backprojection, since in both methods we have to apply filtering for different resolutions. However, the complexity of our algorithm is smaller than Bresler/Delaney's algorithm because of smaller length of projections. If we use linear interpolation at the backprojection part, the total complexity depends on the backprojection part,

which is almost the same in all of the above methods. Fig. 10(b) shows the total complexity of different methods. If, in the backprojection step, we use another method like the nearest neighbor, the total complexity mostly depends on the filtering part and our algorithm can reduce the complexity compared to the method in [9].

VI. SIMULATION RESULTS

We have obtained the wavelet and scaling coefficients of the 256×256 pixel image of the Shepp–Logan head phantom using global data (Fig. 11). In this decomposition, we used the Daubechies' biorthogonal basis [15, Tab. III]. The quality of the reconstructed image is the same as with the filtered backprojection method. Fig. 12 shows an example in which a centered disk of radius 16 pixels is reconstructed using the local reconstruction method proposed in this paper. Fig. 12(c) and (d) shows the blow up of the ROI using both standard filtered backprojection using global data and local reconstruction for comparison. In this example the projections are collected from a disk of radius 28 pixels, therefore the amount of exposure is 22% of the conventional filtered backprojection method. We have observed a constant bias in the reconstructed image, which is natural in the interior reconstruction problem [23], [25]. In the above example, the mean square error (MSE) between the original image and the locally reconstructed image after removing bias is computed over the region of interest.[2] The error energy in the reconstructed image is the same as filtered backprojection method using full exposure data.

---

[2]The MSE is calculated using this equation

$$\frac{1}{N} \sum_{(n,m):(n,m)\in \text{ROI}} (f(n,m) - \hat{f}(n,m))^2$$

where f is the original image, $\hat{f}$ is the reconstructed image with the constant bias removed, and N is the number of pixels in the ROI.
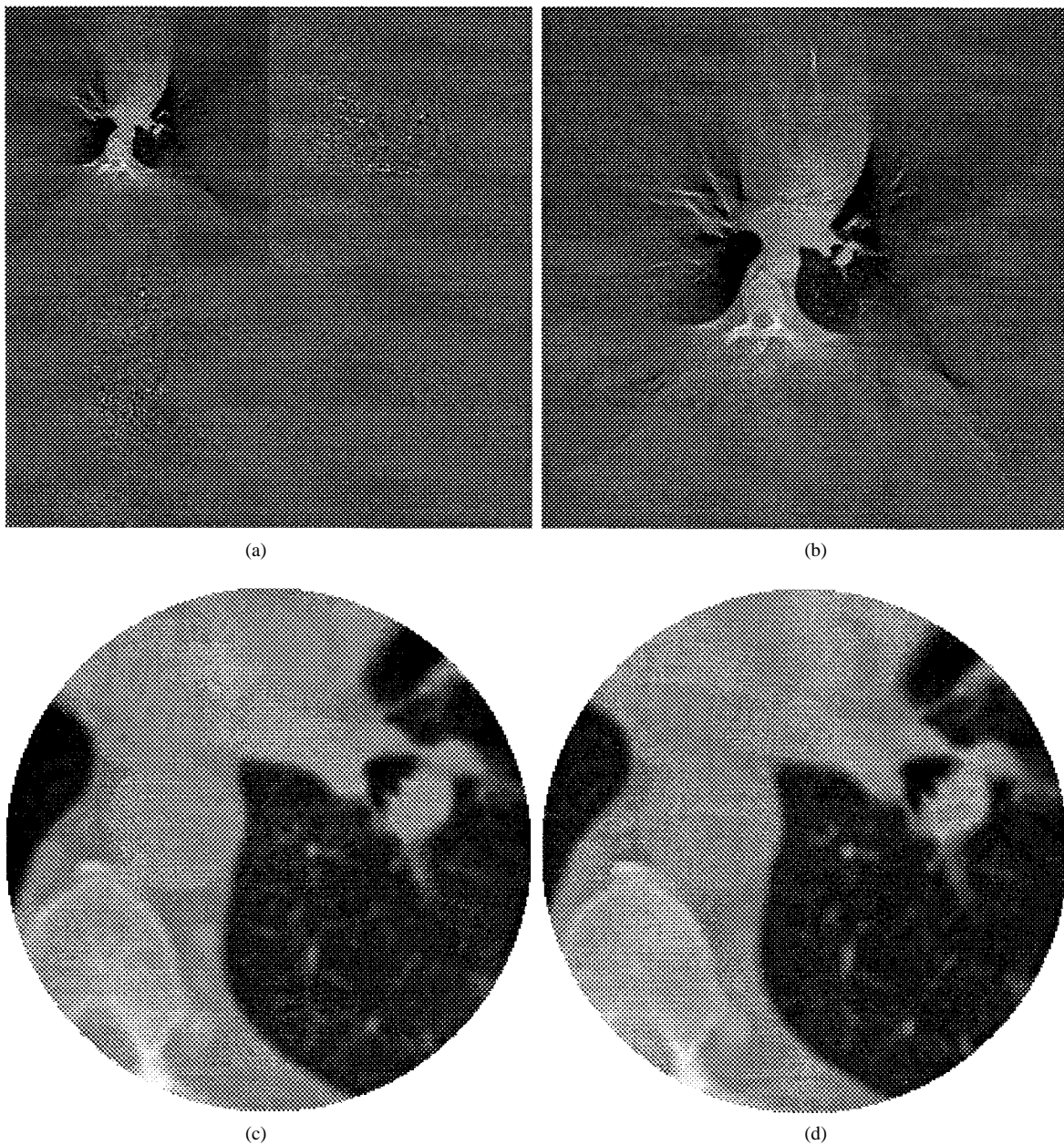
Fig. 14. Local wavelet reconstruction. (a) Wavelet coefficients. (b) Reconstruction from wavelet coefficients; blowup of the ROI. (c) Reconstruction using wavelet method (local data). (d) Reconstruction using standard filtered backprojection method (global data).

The proposed method is applied to the real data obtained from a CT scanner. In the local reconstruction even with 12 pixels extra margin, the reconstructed image has the same quality as the filtered backprojection method. Fig. 13 shows a 1024 × 1024 scan of heart reconstructed from projections sampled at 720 angles over 180° with each projection consisting of 1024 samples covering a recon diameter of 47.5 cm. Using our algorithm, a local centered region of radius 128 pixels of this scan has been reconstructed by using only 27% of exposure (see Fig. 14). The reconstruction in the region of interest is as good as what can be obtained using the filtered backprojection method, which involves global data and 100% exposure. The blow-up of the ROI reconstructed by our local method and global standard filter backprojection is shown in Fig. 14(c) and (d), respectively.

In order to make an accurate comparison with other methods, most notably those described in [8], [9], and [11], we consider two measure criteria for the error in local reconstruction, the maximum relative error (21), and the average relative error. Since most of the error in our reconstructions occurs in a small ring at the boundary of the ROI, the average error is an order of magnitude smaller than the maximum error. This determination is based on the examination of a typical element of the nullspace of the interior Radon transform. Based on the examination of this element, and on other considerations, we fix the size of the margin outside of the region of interest, on which we collect data. In order to limit the maximum error to 1%, we require a margin of 22 pixels, and in order to limit the average error to 1%, we require a margin of 12 pixels (see Fig. 8). Since we are doing extrapolation in

addition to collecting nonlocal data, the actual error is much smaller than the values predicted by examining the nullspace element. Hence, we believe that the 1% average error criterion is the most reasonable in light of the nature of our algorithm. Therefore, the 12-pixel margin is used in our simulations, but we also report comparisons based on the 22-pixel margin.

VII. CONCLUSION

We have developed an algorithm to reconstruct the wavelet and scaling coefficients of a function from its Radon transform. Based on the observation that for some wavelet bases with sufficiently many zero moments, the scaling and wavelet functions have essentially the same support after ramp filtering, we have developed a local reconstruction scheme to reconstruct a local region of a cross section of a body with essentially local data. An upper bound for the local reconstruction error is obtained in terms of the amount of nonlocal data which is used in the reconstruction scheme. Nonuniqueness of the interior problem appears as a constant bias in the reconstructed image. The measured error between the original image and the reconstructed image after removing this bias is negligible. This fact shows that if we use a sufficient amount of nonlocal data in the reconstruction, this bias is reasonably constant on the ROI.

REFERENCES

[1] D. Walnut, "Application of Gabor and wavelet expansions to the Radon transform," in *Probabilistic and Stochastic Methods in Analysis, with Applications*, J. Byrnes, *et al*. Eds. Boston, MA: Kluwer, 1992, pp. 187–205.
[2] C. Berenstein and D. Walnut, "Local inversion of the Radon transform in even dimensions using wavelets," in *75 Years of Radon Transform*, S. Gindikin and P. Michor, Eds. Cambridge, MA: International, 1994, pp. 38–58.
[3] M. Holschneider, "Inverse Radon transforms through inverse wavelet transforms," *Inverse Problems*, vol. 7, 1991, pp. 853–861.
[4] G. Kaiser and Streater, "Windowed Radon transforms," in *Wavelets: A Tutorial in Theory and Applications*, C. K. Chui, Ed. New York: Academic, 1992, pp. 399–441.
[5] A. Faridani *et al.*, "Local and global tomography," in *Signal Processing, IMA* . New York: Springer-Verlag, 1990, vol. 23, pp. 241–255.
[6] A. Faridani, E. Ritman, and K. T. Smith, "Local tomography," *SIAM J. Appl. Math.*, vol. 52, pp. 459–484, Apr. 1992, also, "Examples of local tomography," *SIAM J. Appl. Math.*, vol. 52, pp. 1193–1198, 1992.
[7] A. Faridani, D. Finch, E. L. Ritman, and K. T. Smith, "Local tomography II," *SIAM J. Appl. Math*, vol. 57, pp. 1095–1127, 1997.
[8] J. DeStefano and T. Olson, "Wavelet localization of the Radon transform," *IEEE Trans. Signal Processing*, vol. 42, pp. 2055–2067, Aug. 1994.
[9] A. H. Delaney and Y. Bresler, "Multiresolution tomographic reconstruction using wavelets," in *Proc. IEEE Int. Conf. Image Processing*, vol. ICIP-94, pp. 830–834, Nov. 1994.
[10] J. Destefano and T. Olson, "Wavelet localization of the Radon transform," *IEEE-SP Int. Symp. Time-Frequency and Time-Scale Analysis*, Victoria, BC, Canada, Oct. 1992.
[11] T. Olson, "Optimal time-frequency projections for localized tomography," *Ann. Biomed. Eng.*, vol. 23, pp. 622–636, Sept. 1995.
[12] C. Berenstein and D. Walnut, "Local inversion of the Radon transform in even dimensions using wavelets," GMU Tech. Rep., CAM-21/93, Jan. 1993.
[13] F. Peyrin, M. Zaim, and G. Goutte, "Multiscale reconstruction of tomographic images," in *Proc. IEEE-SP Int. Symp. Time-Frequency Time-Scale Analysis*, 1992.
[14] R. R. Coifman and Y. Meyer, "Remarques sur'l analyze de Fourier 'a fenêtre," *sêrie I. C.R. Acad. Sci. Paris*, vol. 312, pp. 259–261, 1991.
[15] M. Antonini, M. Barlaud, P. Mathieu, and I. Daubechies, "Image coding using wavelet transform," *IEEE Trans. Image Processing*, vol. 1, pp. 205–220, Apr. 1992.
[16] I. Daubechies, *Ten Lectures on Wavelets*. Philadelphia, PA: SIAM, 1992.
[17] S. Mallat, "A theory for multiresolution signal decomposition: The wavelet representation," *IEEE Trans. Pattern Anal. Machine Intell.*, vol. 11, pp. 674–693, July 1989.
[18] K. T. Smith and F. Keinert, "Mathematical foundation of computed tomography," *Appl. Opt.*, vol. 24, pp. 3950–3957, Dec. 1985.
[19] Y. Zhang, M. Coplan, J. Moore, and C. A. Berenstein, "Computerized tomographic imaging for space plasma physics," *J. Appl. Phys.*, vol. 68, pp. 5883–5892, 1990.
[20] G. Beylkin, R. Coifman, and V. Rokhlin, "Fast wavelet transforms and numerical algorithms," *Commun. Pure Appl. Math.*, vol. 44, pp. 141–183, 1991.
[21] J. Guedon and M. Unser, "Least square and spline filtered backprojection," preprint, Mar. 1994.
[22] C. Hamaker, K. T. Smith, D. C. Solomon, and S. L. Wagner, "The divergent beam X-ray transform," *Rocky Mountain J. Math.*, vol. 10, pp. 253–283, 1980.
[23] F. Natterer, *The Mathematics of Computerized Tomography*. New York: Wiley, 1986.
[24] P. Maass, "The interior Radon transform," *SIAM J. Appl. Math*, vol. 52, pp. 710–724, June 1992.
[25] A. K. Louis and A. Rieder, "Incomplete data problem in x-ray computerized tomography," *Numer. Math.*, vol. 56, pp. 371–383, 1989.
[26] A. I. Katsevich and A. G. Ramm, "New methods for finding values of the jumps of a function from its local tomography data," *Inverse Problems*, vol. 11, pp. 1005–1024, 1995.

Farrokh Rashid-Farrokhi (S'88) received the B.S. and M.S. degrees (highest honors) in electrical engineering from Sharif University of Technology, Tehran, Iran, in 1988 and 1992, respectively.

Since 1993, he has been teaching with the Electrical Engineering Department and Institute of Systems Research, University of Maryland, College Park, where he is currently completing the Ph.D. degree. His research interests include array and statistical signal processing, wireless communications and networking, and multiscale image processing.

K. J. Ray Liu (S'86–M'90–SM'93) received the B.S. degree from the National Taiwan University, Taipei, Taiwan, R.O.C., in 1983 and the Ph.D. degree from the University of California, Los Angeles, in 1990, both in electrical engineering.

Since 1990, he has been with the Electrical Engineering Department and Institute for System Research, University of Maryland, College Park, where he is an Associate Professor. During his sabbatical leave in 1996–1997, he was Visiting Associate Professor at Stanford University, Stanford, CA, and Chief Scientist of NeoParadigm Labs. His research interest spans all aspects of signal processing with application to image and video, wireless communications, networking and medical and biomedical technology. He has published over 100 papers, of which more than 30 are in archival journals.

Dr. Liu received numerous awards, including the 1994 National Science Foundation Young Investigator Award, the IEEE Signal Processing Society's 1993 Senior Award (Best Paper Award), the George Corcoran Award, in 1994, for outstanding contributions to electrical engineering education, and the 1995–1996 Outstanding System Engineering Faculty Award in recognition of outstanding contributions in interdisciplinary research, both from the University of Maryland. He is an Associate Editor of IEEE TRANSACTIONS ON SIGNAL PROCESSING, an editor of the *Journal of VLSI Signal Processing,* a member of the Design and Implementation of Signal Processing Systems Technical Committee, and a founding member of Multimedia Signal Processing Technical Committee of the IEEE Signal Processing Society.

Carlos A. Berenstein received the Licenciado en Mathematicas degree from the University of Buenos Aires, Buenos Aires, Argentina, in 1966, and the Ph.D. degree in mathematics from the Courant Institute, New York University, NY, in 1970.

Since 1970, he has taught at Harvard University, Cambridge, MA, Brandeis University, Waltham, MA, and George Mason University, Fairfax, VA. He is currently a Professor of mathematics and a member of the Institute for System Research, University of Maryland, College Park. He has also been a visiting professor at several foreign universities, including the University of Paris, Bordeaux, France, and the Scuola Normale Superior, Pisa, Italy. He has written several monographs and research articles on Fourier analysis, function theory in one and several complex variables, convolution equations, difference-differential equations, boundary value problems, integral, geometry, exponential polynomials and functional analysis, and digital geometry. His current interests include applications of the preceding mathematical theories to tomography, filtering theory, image processing, and complexity theory.

David Walnut received the M.A. degree in 1986 and the Ph.D. degree in 1989, both in mathematics, from the University of Maryland, College Park.

He joined the faculty of George Mason University, Fairfax, VA, in 1990, where he is Associate Professor in the Department of Mathematical Sciences. His research interests include harmonic analysis, wavelet theory, sampling theory, frame theory, deconvolution, and tomography.